

## Modification of HfB<sub>2</sub>–30% SiC UHTC with Graphene (1 vol %) and Its Influence on the Behavior in a Supersonic Air Jet

E. P. Simonenko<sup>a, \*</sup>, N. P. Simonenko<sup>a</sup>, A. F. Kolesnikov<sup>b</sup>, A. V. Chaplygin<sup>b</sup>, A. S. Lysenkov<sup>c</sup>,  
I. A. Nagornov<sup>a, d</sup>, V. G. Sevastyanov<sup>a</sup>, and N. T. Kuznetsov<sup>a</sup>

<sup>a</sup> Kurnakov Institute of General and Inorganic Chemistry, Russian Academy of Sciences, Moscow, 119991 Russia

<sup>b</sup> Ishlinskii Institute of Problems of Mechanics, Russian Academy of Sciences, Moscow, 119526 Russia

<sup>c</sup> Baikov Institute of Metallurgy and Materials Science, Russian Academy of Sciences, Moscow, 119334 Russia

<sup>d</sup> Mendeleev Russian University of Chemical Technology, Moscow, 125047 Russia

\*e-mail: ep\_simonenko@mail.ru

Received May 25, 2021; revised June 6, 2021; accepted June 7, 2021

**Abstract**—Oxidation under exposure to a supersonic dissociated air jet (with heat fluxes in the range 363–779 W/cm<sup>2</sup>, total exposure time: 2000 s) was studied for HfB<sub>2</sub>–30 vol % SiC ultra-high-temperature ceramics (UHTC) doped with a lowered amount (1 vol %) of reduced graphene oxide (GO). Doping the ceramics with a relatively low amount of reduced GO (1 vol %) did not prevent a dramatic increase in the average surface temperature to 2300–2400°C. However, the existence time of surface temperatures below 1800–1850°C increased considerably, probably due to an increase in the thermal conductivity of the ceramics. The ablation rate of the material was determined as 6.5 × 10<sup>−4</sup> g/(cm<sup>2</sup> min), which is intermediate between the respective values for HfB<sub>2</sub>–SiC ceramics and the ceramics doped by 2 vol % graphene. The microstructure features and elemental composition of the oxidized surface and chips of the material were studied. The structure and thickness of the oxidized near-surface region were determined.

**Keywords:** UHTC, graphene, HfB<sub>2</sub>, SiC, oxidation, high-enthalpy air jet, induction plasma torch

**DOI:** 10.1134/S003602362109014X

### INTRODUCTION

Ultra-high-temperature ceramics (UHTC) in the ZrB<sub>2</sub>–SiC and HfB<sub>2</sub>–SiC system are gaining increasing relevance due to the growing amount of knowledge about their properties and the development of new effective methods for their manufacture [1–12]. In addition to their usefulness as materials that can efficiently operate under aerodynamic heating to temperatures above 2000°C [13–17], such ceramics are considered as promising materials for alternative energy sources [18–20], frame components for cermets [21], and other applications. For these materials, however, the set of beneficial properties (high melting points and thermal conductivities, good hardness and bending strength, and high resistance to oxidation, including in supersonic air jet) is deteriorated, in the context of application, by brittleness, which is typical of ceramic materials, and poor resistance to thermal shock (which significantly limits their use in cyclic heating settings).

In order to find a solution to the problem of improving the mechanical properties, studies are currently underway on the doping of MB<sub>2</sub>–SiC (M = Zr, Hf) composite UHTC with components of various chemical nature, e.g., refractory metal carbides, first

of all, Group IV–VIB carbides [22–26], nitrides [27, 28], or oxides that would make it possible to stabilize the tetragonal or cubic phases of oxidation products (ZrO<sub>2</sub>/HfO<sub>2</sub>) [29–31], metals [32–34], etc.

Of particular interest as dopants are carbonaceous materials [35]: continuous or cut reinforcing carbon fibers [36–41], which transfer UHTC to the class of ceramic matrix composites with excellent mechanical properties; carbon nanotubes [42–46]; graphite platelets [47–51] whose strengthening effect is the greater, the smaller the platelet thickness; and graphene [52–58] as an extreme case of very thin graphite platelets.

There is evidence in the literature [56–60] that graphene is a very attractive hardening component for ultra-high-temperature ceramics; due to its properties such as high thermal conductivity, in-plane strength, and specific surface area, graphene makes it possible to significantly increase the strength and resistance to thermal shock (with some inevitable decrease in strength). Moreover, the use of graphene oxide (GO) instead of graphene itself as the carbon component can help to significantly increase the uniformity of graphene distribution in the bulk of ceramics. The  $K_{IC}$  of the ZrB<sub>2</sub>–20 vol % SiC material reaches 7.32 MPa m<sup>1/2</sup> due to doping with 5 vol % GO [57]; the thus-manu-

factured composite also had a very high strength (1055 MPa). An increased fracture toughness while practically maintaining the strength at a level of 940–1050 MPa was also observed with lower graphene doping levels (starting with 0.5 wt %) [56].

Despite this encouraging evidence for an improvement of the mechanical properties of graphene-modified  $\text{ZrB}_2\text{-SiC}$  and  $\text{HfB}_2\text{-SiC}$  ceramics, there are practically no studies of their oxidation resistance. Previously [61] we studied the effect of a supersonic dissociated air jet on  $(\text{HfB}_2\text{-30 vol \% SiC})\text{-2 vol \% C}_G$  composite UHTC that was manufactured by sol-gel technology and the reactive hot pressing of  $\text{HfB}_2\text{-(SiO}_2\text{-C)-rGO}$  powders, where *rGO* stands for reduced graphene oxide. An even as low amount as 2 vol % graphene prevented the onset of a sharp heating of the sample surface to temperatures of 2300–2700°C (the so-called temperature jump [62]), likely, due to a higher thermal conductivity. It was due to a reduced surface temperature, which did not exceed 1685°C during the entire time of exposure (2000 s), that there were a significant (by one order of magnitude) decrease in the thickness of the oxidized near-surface layer and a threefold reduction in the ablation rate per unit surface.

Such a significant change in the oxidation behavior of UHTC due to doping with as little as two volume percent graphene led us to the idea of the practical significance of studying whether the dopant amount can be reduced further.

The goals of the work presented here were to manufacture  $(\text{HfB}_2\text{-30 vol \% SiC})\text{-1 vol \% C}_G$  UHTC material and to study its oxidation behavior under exposure to a supersonic dissociated air jet.

## EXPERIMENTAL

The reagents used were tetraethoxysilane  $\text{Si}(\text{OC}_2\text{H}_5)_4$  (specialty grade, EKOS-1), LBS-1 bake-lite varnish (carbolite), formic acid  $\text{CH}_2\text{O}_2$  (>99%, Spektr-Khim), hafnium diboride (>98%, particle size ~2–3 μm, aggregate size ~20–60 μm, Refractory Materials), and graphene oxide (platelet size ≤3 μm, graphene layers ≤2, AkkoLab).

The method for manufacturing the UHTC containing  $\text{HfB}_2\text{-30 vol \% SiC}$  and doped with reduced graphene oxide is described in detail elsewhere [61]. For manufacturing  $\text{HfB}_2\text{-(SiO}_2\text{-C)-rGO}$  composite powders, for example, the procedure was as follows: the graphene oxide powder was dispersed and formic acid and tetraethoxysilane were dissolved in an ethanol solution of phenol-formaldehyde resin (the polymer carbon source). Then, tetraethoxysilane hydrolysis was initiated, and the  $\text{HfB}_2$  powder was dispersed in the resulting colloidal solution. After gelation and drying in a rotary evaporator, the xerogel was heat-treated under a dynamic vacuum at 400°C to pyrolyze its

organic components and form reduced graphene oxide.

For manufacturing  $\text{HfB}_2\text{-SiC-C}_G$  ceramics, the composite powder was consolidated in graphite molds using a Thermal Technology (model HP20-3560-20) hot press at 1800°C (heating rate 10 K/min, exposure time 15 min) and a pressure of 30 MPa [9–11, 15].

The oxidation resistance of the thus-manufactured  $(\text{HfB}_2\text{-30 vol \% SiC})\text{-1 vol \% C}_G$  material under exposure to a supersonic dissociated air jet was studied on a VGU-4 100-kW RF induction plasma torch using a sonic nozzle with an outlet diameter of 30 mm. The distance from the nozzle to the sample was 25 mm, the air jet rate was 3.6 g/s, and the chamber pressure was 13–14 hPa. A sample shaped as a cylinder 15 mm long and ~3.6 mm thick was inserted into a high-enthalpy air jet at a torch anode supply power (*N*) of 30 kW, and the supply power was then stepwise increased to 70 kW in 10-kW steps. The exposure time at each step (with *N* = 30–60 kW) was 2 min; once *N* = 70 kW was reached, the sample was exposed until the experiment was over; the total exposure time was 33 min 20 s (2000 s).

The geometry of experiment provided the 1 mm excursion of the sample relative to the face of the water-cooled copper unit [8–10, 15]. In order to improve the fixation of the sealant (which was used as strips of paper based on fibrous SiC), the strips were placed in a frame made of copper foil, which slightly increased the heat transfer from the sample to the unit compared to the previously described experiments.

The average surface temperature of the heated sample was measured on a Mikron M-770S infrared pyrometer in the spectral ratio pyrometer mode (the temperature range 1000–3000°C, the sighting area diameter: ~5 mm in the central part of the sample). A VS-415U Tandem thermal imager was used to study the temperature distribution over the sample surface. Thermal images were recorded at a set value of the spectral emissivity  $\epsilon$  at the wavelength 0.9 μm, equal to 0.6. If necessary, the surface temperature values were corrected for real  $\epsilon$  values during thermal imager data analysis.

X-ray diffraction patterns were recorded from the surfaces of samples on a Bruker D8 Advance diffractometer ( $\text{CuK}_\alpha$  radiation, resolution: 0.02°, signal accumulation time per point: 0.3 s). Phase identification was in MATCH! – Phase Identification from Powder Diffraction software, Version 3.8.0.137 (Crystal Impact) with the integrated Crystallography Open Database (COD).

The microstructure features of the oxidized surface and chips of the sample were studied using scanning electron microscopy (SEM) on an NVision 40 (Carl Zeiss) three-beam workstation at an accelerating voltage of 1 and 20 kV. The elemental composition in areas was determined with an X-MAX 80 Oxford Instruments energy-dispersive microprobe analyzer unit.

## RESULTS AND DISCUSSION

Table 1 shows the variation in average surface temperature (as measured by a pyrometer) depending on the anode supply power and the chamber pressure. The above-mentioned heat fluxes to the water-cooled copper calorimeter ( $q$ ) were determined beforehand in separate experiments as described elsewhere [63], and varied from 363 W/cm<sup>2</sup> ( $N = 30$  kW) to 779 W/cm<sup>2</sup> ( $N = 70$  kW).

Figure 1 shows the variation in surface temperature of the sample during the experiment in comparison to the data obtained for HfB<sub>2</sub>-30 vol % SiC and (HfB<sub>2</sub>-30 vol % SiC)-2 vol % C<sub>G</sub> samples [61] with the same exposure to a supersonic high-enthalpy air jet. All samples exhibit similar trends in the surface temperature in response to increasing anode power supply (up to 500 s of exposure): as  $N$  increases stepwise, the temperature rises in correspondence. At the same time, in the ceramics doped with one volume percent graphene, the surface temperature at a power of 30–50 kW is only slightly lower than for the undoped HfB<sub>2</sub>-30 vol % SiC sample (Fig. 1, red curve). When  $N = 60$  kW, the behavior of the material becomes similar to the behavior of the (HfB<sub>2</sub>-30 vol % SiC)-2 vol % C<sub>G</sub> material (Fig. 1, green curve): at a fixed power, the surface temperature practically does not change with time, while for the HfB<sub>2</sub>-30 vol % SiC material it starts to increase.

When the power reaches the maximal value (70 kW) for the (HfB<sub>2</sub>-30 vol % SiC)-1 vol % C<sub>G</sub> material (Fig. 1, violet curve), three segments with differing slopes may be distinguished on the curve. Over a time interval of 495–770 s, the temperature practically does not increase (1632 → 1642°C); its variation rate is ~2 K/min. Starting at 770 and up to 1540 s, the temperature elevation rate increases slightly to 13 K/min, as a result of which the surface acquires a temperature of ~1800°C. Subsequent exposure at  $N = 70$  kW leads to a break in the temperature curve; the heating rate increases dramatically to 73 K/min.

Materials with different graphene contents, which obviously determines the thermal conductivity of ceramics as a whole, have different rates to reach an average surface temperature of 1800°C, followed by a rather rapid heating of the surface to ~2400–2500°C: 16 K/min (0 vol % C<sub>G</sub>) → 13 K/min (1 vol % C<sub>G</sub>) → 5.4 K/min (2 vol % C<sub>G</sub>). That is, for the (HfB<sub>2</sub>-30 vol % SiC)-2 vol % C<sub>G</sub> sample having the highest graphene amount, the surface temperature has not increased to the critical value (1800°C) because of the rather low rate (5.4 K/min). For the undoped material, the temperature jump was observed after exposure to  $N = 70$  kW for ~570 s (9.5 min). Doping the ceramics with as little as one volume percent of graphene made it possible to stretch this time interval almost twofold to about 1030 s (17 min).

**Table 1.** Variations in average surface temperature of a (HfB<sub>2</sub>-30 vol % SiC)-1 vol % C<sub>G</sub> sample in the vicinity of the critical point (a spectral ratio pyrometer,  $T$ ) as dependent on the exposure time and process parameters: the anode supply power ( $N$ ) and chamber pressure in the plasma torch (13.8–14.2 hPa), and relevant heat fluxes ( $q$ )

Time, min	$N$ , kW	$q$ , W/cm <sup>2</sup>	$T$ , °C
0 → 2	30	363	1293 → 1260
2 → 4	40	484	1363 → 1358
4 → 6	50	598	1445 → 1446
6 → 8	60	691	1531 → 1536
8	70	779	1625 → 1628
10	70	779	1626
15	70	779	1677
20	70	779	1750
23	70	779	1798
25	70	779	1810
26	70	779	1834
27	70	779	1916
28	70	779	1998
29	70	779	2076
30	70	779	2157
31	70	779	2248
32	70	779	2305
33.20	70	779	2368

Heat fluxes toward the water-cooled copper calorimeter were determined in separate experiments described in [63].

The study of surface temperature distribution at various moments of exposure confirms the pyrometer measurement data (Figs. 2–4). In Figs. 2 and 3 one can observe a systematic rise in temperature, which is very uniformly distributed over the surface of the sample, at the initial stages of exposure to a supersonic air jet. In the progress of exposure (Fig. 3), after 25 min (>1500 s) local surface areas where the temperature is far higher than the average value appear as a result of gradual evaporation of the silicate glass protective layer from the surface (Fig. 3, experiment 1545 s). The appearance of these overheated foci further accelerates evaporation of the protective vitreous layer from the surface, to give rise to a break on the average temperature curve (Fig. 1). Subsequent exposure leads to an increase in the area and temperature of overheated surface areas, among other reasons due to the formation of bulges, i.e., bubbles, which are formed around dispersed unbound HfO<sub>2</sub> particles, spontaneously structured as a result of the abrupt evaporation of silicate glass components from the oxidized near-surface region of the composite.

Of particular interest is how the sample surface cools when heating is turned-off. It is due to the active heat removal by the conductive mechanism that over-

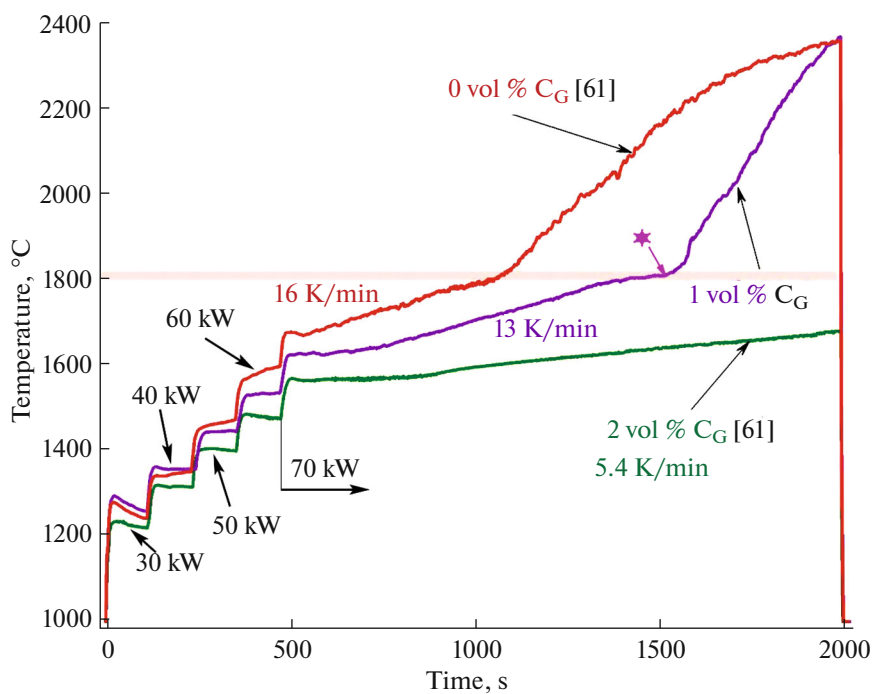


**Fig. 1.** Variation in average surface temperature for a  $(\text{HfB}_2\text{-30 vol \% SiC})\text{-1 vol \% C}_G$  sample against that for  $\text{HfB}_2\text{-30 vol \% SiC}$  and  $(\text{HfB}_2\text{-30 vol \% SiC})\text{-2 vol \% C}_G$  ceramics [61].

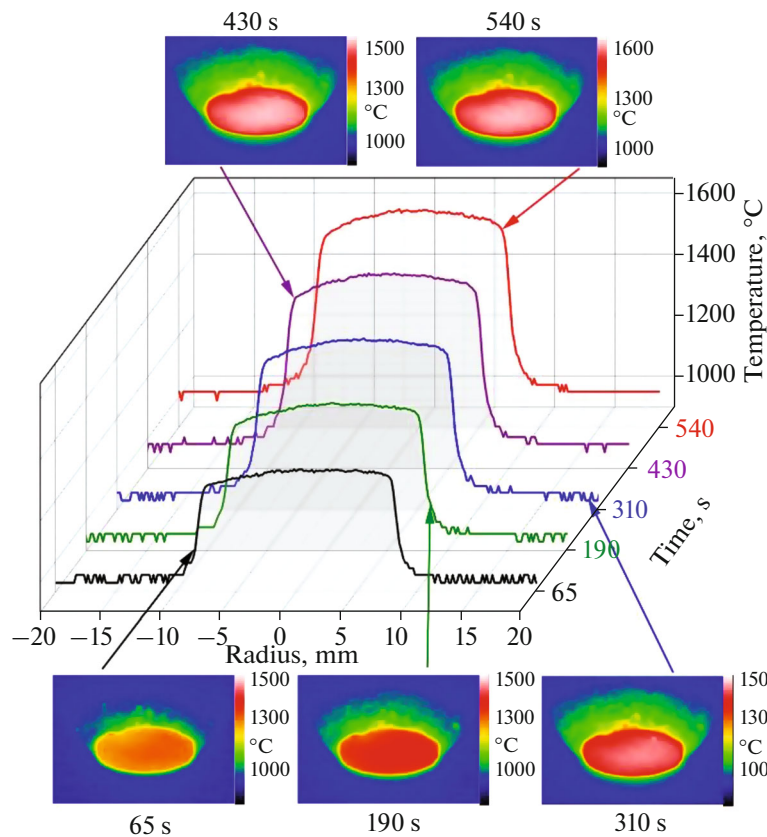


**Fig. 2.** Thermal images and their corresponding temperature distributions along the diameter of a  $(\text{HfB}_2\text{-30 vol \% SiC})\text{-1 vol \% C}_G$  sample upon a stepwise increase in plasma torch anode supply power from 30 to 70 kW (experiment, 1–540 s).

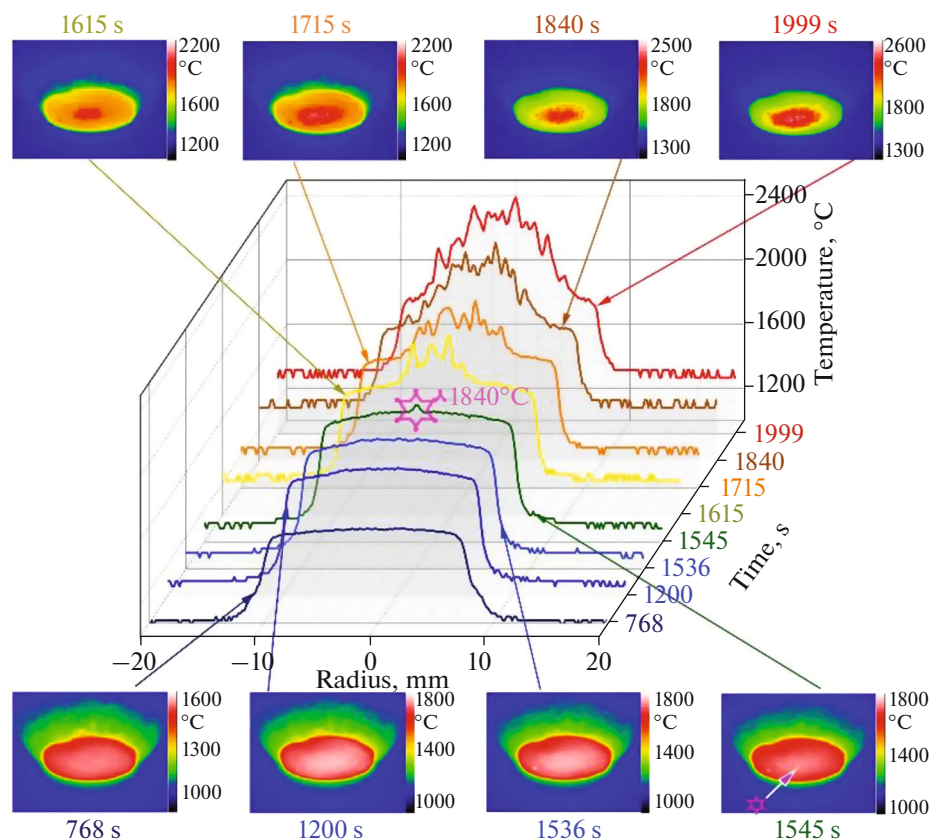


**Fig. 3.** Thermal images and their corresponding temperature distributions along the diameter in a (HfB<sub>2</sub>-30 vol % SiC)-1 vol % C<sub>G</sub> sample under exposure to plasma torch with an anode supply power of 70 kW (experiment, 768–1999 s).

heated areas disappear as soon as in the next second after the heating is turned-off, so the temperature distribution is evened out over the entire surface (Fig. 4).

The weight loss of the sample upon exposure to a supersonic dissociated air jet was 0.4%; the respective ablation rate (Fig. 5) was  $6.5 \times 10^{-4}$  g/(cm<sup>2</sup> min). Although this value is intermediate between the respective values for HfB<sub>2</sub>-30 vol % SiC and (HfB<sub>2</sub>-30 vol % SiC)-2 vol % C<sub>G</sub> materials after similar exposure [61], it is yet closer to the value obtained for the ceramics doped with 2 vol % graphene. This is probably due to the lesser degradation in shorter exposure times at temperatures above 1800–2000 °C.

The X-ray powder diffraction patterns recorded from the oxidized surface of the (HfB<sub>2</sub>-30 vol % SiC)-1 vol % C<sub>G</sub> (Fig. 6) sample evidence that the surface phase composition corresponds with that of undoped HfB<sub>2</sub>-30 vol % SiC [61]; the only crystalline oxidation product in this case is monoclinic hafnium oxide [64] with slightly increased unit cell parameters. Obviously, this is due to the following: in both cases, the samples were subjected to prolonged exposure to temperatures above 1800–2000 °C, which led to intensive evaporation of silicate glass components from the surface. Probably, it is just due to the high surface tem-

peratures of the (HfB<sub>2</sub>-30 vol % SiC)-1 vol % C<sub>G</sub> sample that the sample does not contain a crystalline boric acid phase [65], which was detected on the surface of the (HfB<sub>2</sub>-30 vol % SiC)-2 vol % C<sub>G</sub> sample after the test (where the temperature did not exceed 1685 °C).

The microstructure of the oxidized surface also significantly resembles that of undoped HfB<sub>2</sub>-30 vol % SiC (Figs. 7 and 8). Since at the final stages of heating there was a significant temperature difference between the central and peripheral areas, these areas were analyzed separately. Hafnium oxide was the major surface species as probed by EDX analysis (Table 2).

In general, the surface is a porous ceramic crust, on the surface of which there are large bulges and pits from ruptured bubbles having diameters up to 400–700 μm. These items, apparently, appeared as a result of the accumulation of gaseous oxidation products in a silicate glass layer located in the near-surface region and having a relatively low viscosity due to elevated temperatures. These pits have their bottoms consisting mainly of a molten glassy phase, and on the walls, one can notice a gradual increase in the proportion of HfO<sub>2</sub> particles wetted with silicate glass (Figs. 7b, 7e, and 7f). As the distance from the center of the sample

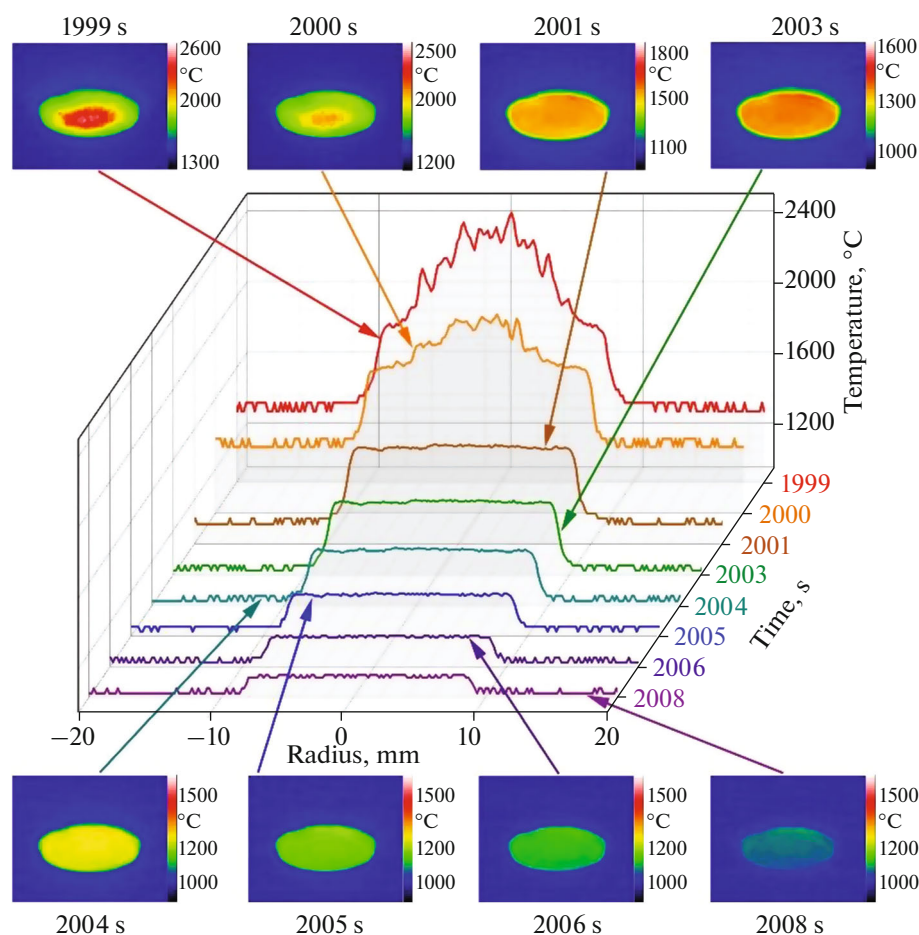


**Fig. 4.** Thermal images and their corresponding temperature distributions along the diameter in a  $(\text{HfB}_2\text{-30 vol \% SiC})\text{-1 vol \% C}_G$  sample under cooling after heating is switched off (experiment, 1999–2008 s).

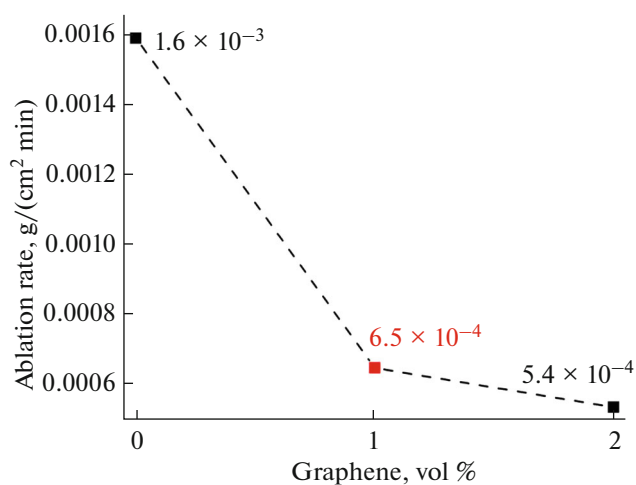


**Fig. 5.** Ablations rates of UHTC after long-term (2000 s) exposure to a supersonic dissociated air jet; for the samples containing 0 and 2 vol % graphene, data are borrowed from [61].

increases and, accordingly, the surface temperature decreases (while being no lower than 1830–1870 °C even at the very edge of the sample), the number of large bulges and their diameter decrease (<250 μm), and the pits from bursting bubbles completely disappear. Only relatively small items ~30 μm in diameter remain on the surface.

It is likely due to the number of burst bubbles the inner side of which has a high SiO<sub>2</sub> content decreasing to the edge of the  $(\text{HfB}_2\text{-30 vol \% SiC})\text{-1 vol \% C}_G$  sample, that the ratio  $n(\text{Hf}) : n(\text{Si})$  on the surface increases in going from the central area to the periphery.

The body of elemental analysis data of oxidized surfaces of  $(\text{HfB}_2\text{-30 vol \% SiC})\text{-}x \text{ vol \% C}_G$  ( $x = 0, 1, \text{ or } 2$ ) samples in light of information from [61] supports the following logical and obvious conclusion: the higher the surface temperature was and the longer time it exceeded 1800 °C, the higher is the ratio  $n(\text{Hf}) : n(\text{Si})$  on the oxidized surface in the central area, for those settings enhance the evaporation of silicate glass components.

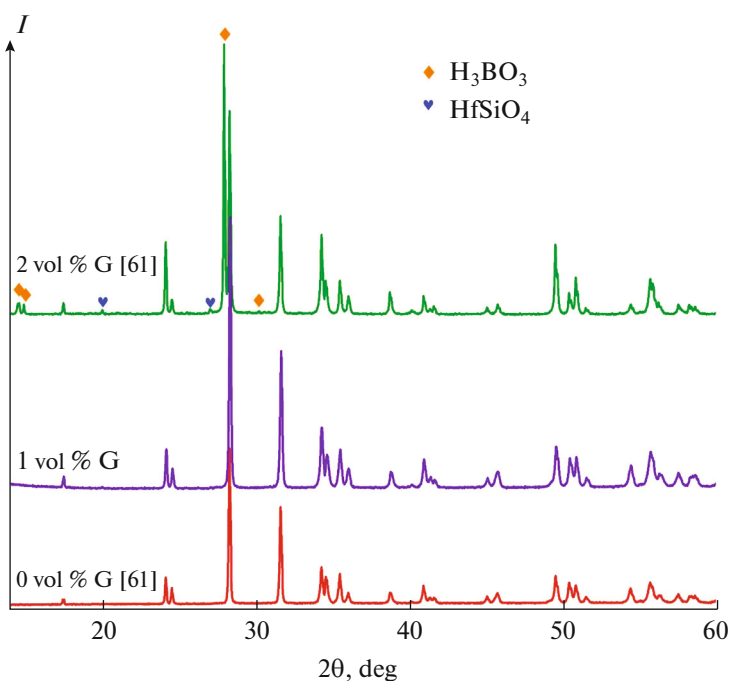


**Fig. 6.** X-ray diffraction patterns of the oxidized surface of a (HfB<sub>2</sub>-30 vol % SiC)-1 vol % C<sub>G</sub> sample against those for HfB<sub>2</sub>-30 vol % SiC and (HfB<sub>2</sub>-30 vol % SiC)-2 vol % C<sub>G</sub> ceramics [61].

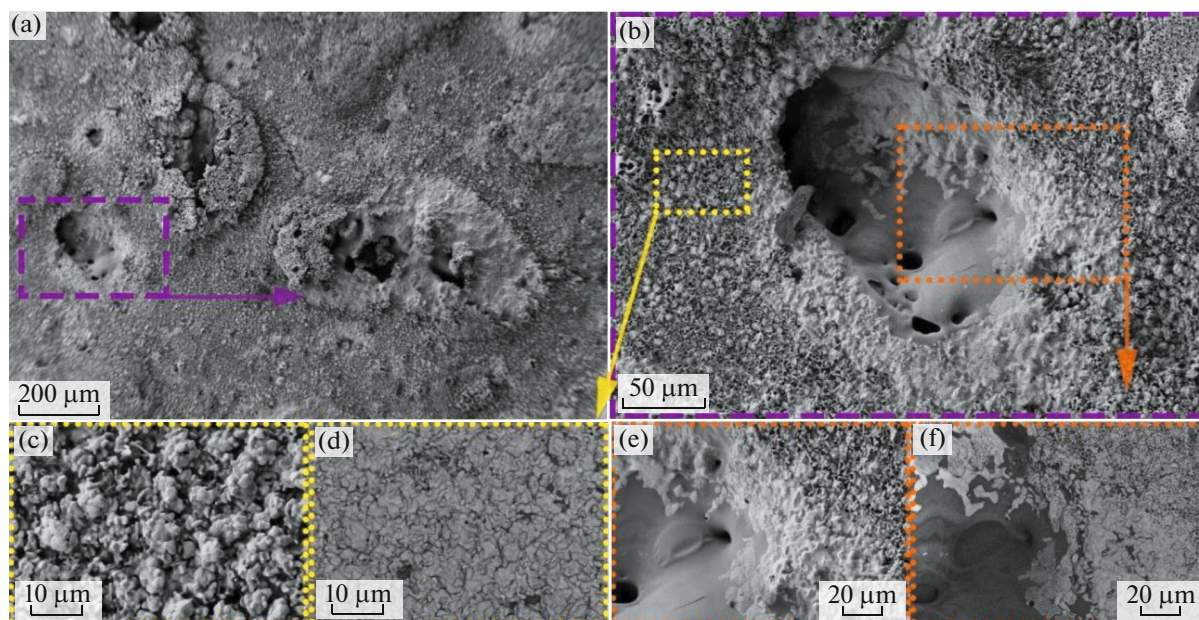


**Fig. 7.** Microstructure of the oxidized surface of an (HfB<sub>2</sub>-30 vol % SiC)-1 vol % C<sub>G</sub> sample in the central area (as probed by SEM): (a, b, c, e) in the backscattered electron mode and (d, f) in the atomic number contrast mode; the accelerating voltage: 1 kV.

The study of a cleaved surface (Fig. 9) indicates that the total thickness of the oxidized layer in the central area is far smaller than for the HfB<sub>2</sub>-30 vol % SiC sample [61], and is 200–250 μm. In this case, it is possible to clearly distinguish not only the upper oxidized layer, which is a melt of silicate glass, over which

weakly bound and relatively fine HfO<sub>2</sub> particles are distributed (Figs. 9b and 9e), but also a porous, silicon carbide-depleted layer. A higher accelerating voltage of 20 kV (Fig. 10) enabled us to discover that the uneven relief of the oxidized surface and the bulges are formed exclusively due to the formation of gas bubbles

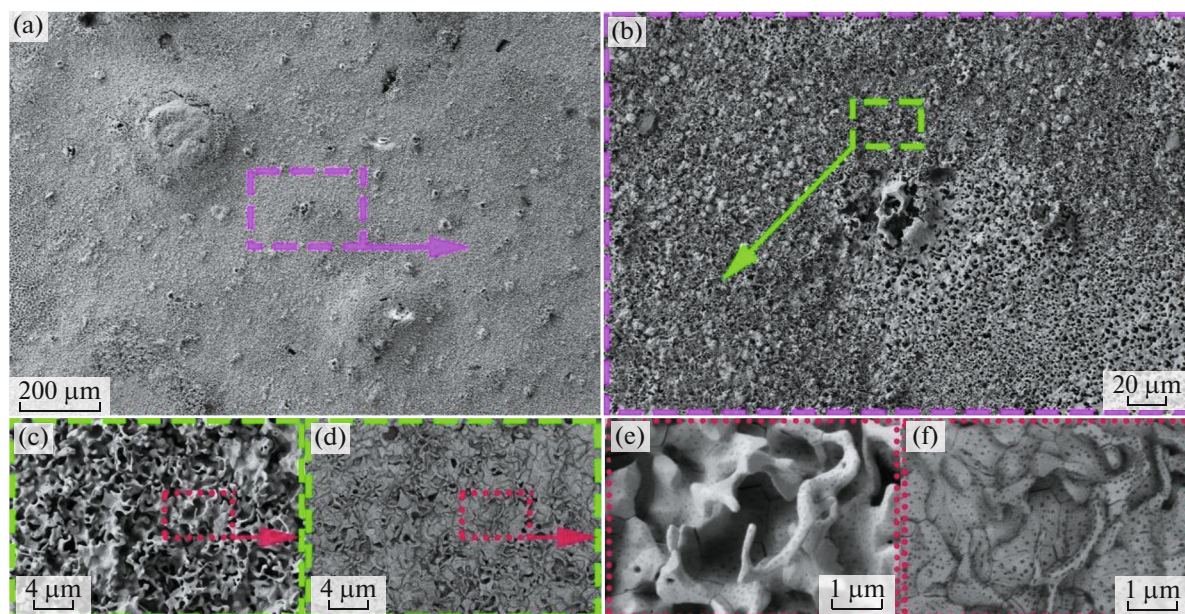


**Fig. 8.** Microstructure of the oxidized surface of a  $(\text{HfB}_2\text{-30 vol \% SiC})\text{-1 vol \% C}_G$  sample in the peripheral area (as probed by SEM): (a, b, c, e) in the backscattered electron mode and (d, f) in the atomic number contrast mode; the accelerating voltage: 1 kV.

in the thin interlayer between the SiC-depleted layer and the upper layer, which is dominated by  $\text{HfO}_2$  particles bound to one another by silicate melt. The  $\text{HfO}_2$  particles have a narrow particle size distribution in the melt; their sizes range from  $\sim 0.5\text{--}0.9\ \mu\text{m}$  for near-spherical particles to vertically oriented druses up to  $5\text{--}6\ \mu\text{m}$  in length and up to  $2.5\text{--}3\ \mu\text{m}$  in diameter. Their proportion relative to the silicate phase increases with approaching the surface (Fig. 9d). The thickness of this movable upper layer is  $\sim 40\text{--}60\ \mu\text{m}$ .

The thickness of the underlying SiC-depleted layer is on the order of  $100\text{--}110\ \mu\text{m}$ . However, as one can see in Figs. 9f and 9g, the most porous layer  $\sim 60\text{--}90\ \mu\text{m}$

thick can be conditionally distinguished here (Figs. 9j and 9k), below which the density of the material gradually increases, passing into unoxidized ceramics (Figs. 9h and 9i).

Comparative analysis shows the following (Table 2): despite the close average surface temperatures by the end of long-term (2000 s) exposure to a supersonic dissociated air jet, there is no so much difference between the thicknesses of the upper oxidized silicate glass layers, with  $\text{HfO}_2$  particles distributed therein, in the central areas of the  $\text{HfB}_2\text{-30 vol \% SiC}$  and  $(\text{HfB}_2\text{-30 vol \% SiC})\text{-1 vol \% C}_G$  samples, whereas the porous SiC-depleted layer becomes more than two

**Table 2.** Ratios  $n(\text{Hf}) : n(\text{Si})$  (as probed by EDX) in the central and peripheral surface areas of the  $(\text{HfB}_2\text{-30 vol \% SiC})\text{-1 vol \% C}_G$  material after exposure to a supersonic dissociated air jet, and the oxidized layer thickness in the central area against the values for the unmodified materials and the material doped with 2 vol % graphene [61]

Sample	Surface temperature in the end of thermochemical exposure, °C*	$n(\text{Hf}) : n(\text{Si})$		Oxidized layer thickness (in central area), $\mu\text{m}$		
		in central area	in peripheral area	silicate glass with embedded $\text{HfO}_2$ particles	SiC-depleted area	total
$\text{HfB}_2\text{-30 vol \% SiC}$ [61]	2360	14.9	16.7	45–130	230–245	280–400
<b><math>(\text{HfB}_2\text{-30 vol \% SiC})\text{-1 vol \% C}_G</math></b>	<b>2370</b>	<b>6.9</b>	<b>38.0</b>	<b>40–60</b>	<b>100–110</b>	<b>200–250</b>
$(\text{HfB}_2\text{-30 vol \% SiC})\text{-2 vol \% C}_G$ [61]	1680	1.3	2.1	20–30	0–15	20–45

\* In the central area as measured by a spectral ratio pyrometer.



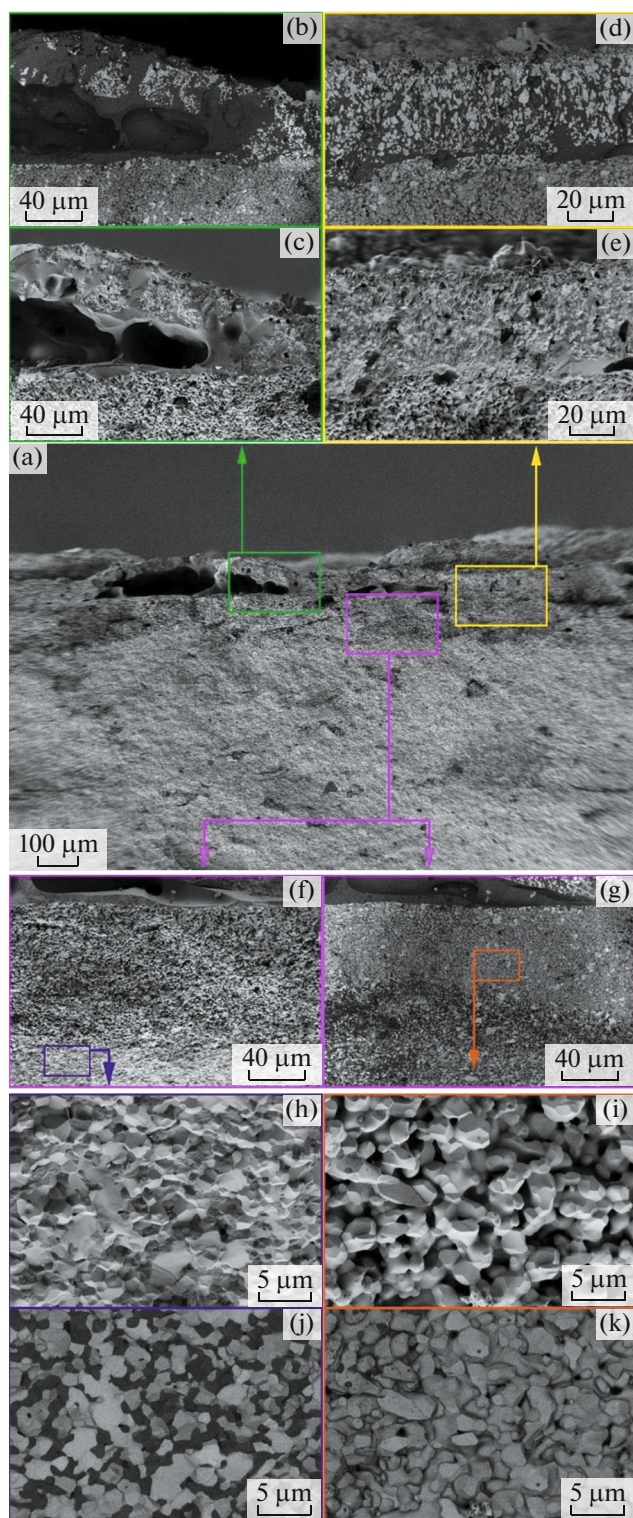


**Fig. 9.** Microstructure of a cleaved ( $\text{HfB}_2$ -30 vol % SiC)-1 vol %  $\text{C}_G$  sample after thermochemical exposure (as probed by SEM): (a, c, e, f, h, j) in the backscattered electron mode and (b, d, g, i, k) in the atomic number contrast mode; the accelerating voltage: 1 kV.



**Fig. 10.** Microstructure of a cleaved ( $\text{HfB}_2$ -30 vol % SiC)-1 vol %  $\text{C}_G$  sample after thermochemical exposure (as probed by SEM); the accelerating voltage: 1 kV.

times thinner due to doping with only 1 vol% graphene. It should be mentioned, however, that an increase in the graphene content to 2 vol % makes it possible to reduce the total thickness of the oxidized layer by one order of magnitude. This effect clearly demonstrates the destructive effect on the oxidation resistance of the material caused by a temperature jump to values higher than 1800–2000°C, due to the attendant sharp increase in the intensity of evaporation of the components of protective silicate glass. In this case, it was probably the long duration of exposure that promoted deeper oxidation of the ( $\text{HfB}_2$ -30 vol % SiC)-1 vol %  $\text{C}_G$  material.

## CONCLUSIONS

$\text{HfB}_2$ -30 vol % SiC ultra-high-temperature ceramics doped with 1 vol % of reduced graphene oxide have been manufactured by sol-gel technology and reactive hot pressing.

The oxidation of the thus-manufactured ceramics has been studied under long-term (2000 s) exposure to a supersonic dissociated air jet (the heat flux varied in the range 363–779  $\text{W}/\text{cm}^2$ ).

A relatively low doping level with reduced graphene oxide (1 vol %) has not prevented the dramatic rise in average surface temperature to 2300–2400°C in  $\text{HfB}_2$ -30 vol % SiC ceramics. However, this doping gives an opportunity to stretch the existence range of surface temperatures lower than 1800–1850°C (the onset of temperature jump with an intense evaporation of silicate glass) from ~18 to 25 min, likely due to the increasing thermal conductivity of the ceramics. Thus, the oxidation time of ceramics during which the surface temperature exceeds 1800°C (which leads to the most significant degradation of the material), has been reduced by almost two times, from 15 min (in  $\text{HfB}_2$ -30 vol % SiC ceramics [61]) to 8 min (in ( $\text{HfB}_2$ -30 vol % SiC)-1 vol %  $\text{C}_G$  ceramics).

This heating protocol has led to a significant decrease in the ablation rate of the material from  $1.6 \times 10^{-3}$  g/(cm<sup>2</sup> min) [61] to  $6.5 \times 10^{-4}$  g/(cm<sup>2</sup> min), the latter being rather closer to the values measured for (HfB<sub>2</sub>-30 vol % SiC)-2 vol % C<sub>G</sub> ceramics ( $5.4 \times 10^{-4}$  g/(cm<sup>2</sup> min) [61]).

An about twofold decrease in the overall thickness of the oxidized layer has been achieved in the manufactured (HfB<sub>2</sub>-30 vol % SiC)-1 vol % C<sub>G</sub> ceramics. However, those values are yet noticeably higher than for ceramics doped with 2 vol % graphene, likely due to high-temperature exposure at temperatures above 1800–2000°C.

It may be assumed that, if the exposure time to a supersonic dissociated air jet were shortened to 20–25 min, the degradation of the ceramics would have been far lower.

In general, we may conclude that an even very low graphene doping level (1 vol %) is efficient in HfB<sub>2</sub>-30 vol % SiC ultra-high-temperature ceramics. In this case, however, it is advisable to keep in mind a shortened time of existence of the ceramics with the least degradation.

#### ACKNOWLEDGMENTS

The study of the evolution of the microstructure and phase composition of the samples as a result of oxidation was carried out using the equipment of the Center for Shared Use of Physical Methods for Researching Substances and Materials of the Kurnakov Institute RAS, which was supported by the Ministry of Science and Higher Education of the Russian Federation as part of the State Assignment of the Kurnakov Institute of General and Inorganic Chemistry, Russian Academy of Sciences.

#### FUNDING

The studies of the thermochemical behavior of graphene-doped samples was supported by the Russian Foundation for Basic Research (project No. 20-01-00056). The experiment on a VGU-4 MW plasma torch was in part supported by the Government assignment to the Ishlinskii Institute of Problems of Mechanics (project No. AAAA-A20-120011690135-5: modification of measurement systems).

#### CONFLICT OF INTEREST

The authors declare that they have no conflicts of interest.

#### REFERENCES

1. E. P. Simonenko, N. P. Simonenko, V. G. Sevast'yanov, et al. *Ultra-High-Temperature Ceramic Materials: Current Problems and Trends* (IP Konyakhin A. V. (Book Jet), Moscow, 2020) [in Russian].
2. E. P. Simonenko, D. V. Sevast'yanov, N. P. Simonenko, et al., *Russ. J. Inorg. Chem.* **58**, 1669 (2013). <https://doi.org/10.1134/S0036023613140039>
3. X. Ma, C. Wei, R. Liu, et al., *Corros. Sci.* **182**, 109283 (2021). <https://doi.org/10.1016/j.corsci.2021.109283>
4. B. Mohammadzadeh, S. Jung, T. H. Lee, et al., *Ceram. Int.* **47**, 11438 (2021). <https://doi.org/10.1016/j.ceramint.2020.12.271>
5. R. Hassan and K. Balani, *Corros. Sci.* **177**, 109024 (2020). <https://doi.org/10.1016/j.corsci.2020.109024>
6. S. Jafari, M. Bavand-Vandchali, M. Mashhadi, et al., *Int. J. Refract. Met. Hard Mater.* **94**, 105371 (2021). <https://doi.org/10.1016/j.ijrmhm.2020.105371>
7. C. Xia, S. A. Delbari, Z. Ahmadi, et al., *Ceram. Int.* **46**, 29334 (2020). <https://doi.org/10.1016/j.ceramint.2020.08.054>
8. E. P. Simonenko, N. P. Simonenko, A. N. Gordeev, et al., *Russ. J. Inorg. Chem.* **65**, 606 (2020). <https://doi.org/10.1134/S0036023620040191>
9. E. P. Simonenko, N. P. Simonenko, A. S. Mokrushin, et al., *Russ. J. Inorg. Chem.* **64**, 1849 (2019). <https://doi.org/10.1134/S0036023619140109>
10. E. P. Simonenko, N. P. Simonenko, A. N. Gordeev, et al., *J. Sol-Gel Sci. Technol.* **92**, 386 (2019). <https://doi.org/10.1007/s10971-019-05029-9>
11. E. P. Simonenko, N. P. Simonenko, E. K. Papynov, et al., *Russ. J. Inorg. Chem.* **63**, 1 (2018). <https://doi.org/10.1134/S0036023618010187>
12. C. Piriou, O. Rapaud, S. Foucaud, et al., *Ceram. Int.* **45**, 1846 (2019). <https://doi.org/10.1016/j.ceramint.2018.10.075>
13. S. Mungiguerra, G. D. Di Martino, R. Savino, et al., *Int. J. Heat Mass Transfer* **163**, 120492 (2020). <https://doi.org/10.1016/j.ijheatmasstransfer.2020.120492>
14. K. Vaferi, M. Vajdi, S. Nekahi, et al., *Ceram. Int.* **47**, 567 (2021). <https://doi.org/10.1016/j.ceramint.2020.08.164>
15. E. P. Simonenko, N. P. Simonenko, A. N. Gordeev, et al., *J. Eur. Ceram. Soc.* **40**, 1093 (2020). <https://doi.org/10.1016/j.jeurceramsoc.2019.11.023>
16. B. Mohammadzadeh, S. Jung, T. H. Lee, et al., *Materials (Basel)* **13**, 2213 (2020). <https://doi.org/10.3390/ma13102213>
17. R. Mukherjee and B. Basu, *Adv. Appl. Ceram.* **117**, S2 (2018). <https://doi.org/10.1080/17436753.2018.1509169>
18. L. Silvestroni, D. Sciti, L. Zoli, et al., *Renew. Energy* **133**, 1257 (2019). <https://doi.org/10.1016/j.renene.2018.08.036>
19. Q. Lonné, N. Glandut, and P. Lefort, *J. Eur. Ceram. Soc.* **32**, 955 (2012). <https://doi.org/10.1016/j.jeurceramsoc.2011.10.027>
20. C. Musa, R. Licheri, R. Orrù, et al., *Sol. Energy* **169**, 111 (2018). <https://doi.org/10.1016/j.solener.2018.04.036>
21. Y. Qi, K. Jiang, C. Zhou, et al., *J. Eur. Ceram. Soc.* **41**, 2239 (2021). <https://doi.org/10.1016/j.jeurceramsoc.2020.11.009>
22. P. Sengupta, S. S. Sahoo, A. Bhattacharjee, et al., *J. Alloys Compd.* **850**, 156668 (2021). <https://doi.org/10.1016/j.jallcom.2020.156668>

23. E. P. Simonenko, N. P. Simonenko, A. N. Gordeev, et al., *J. Eur. Ceram. Soc.* **41**, 1088 (2021).  
<https://doi.org/10.1016/j.jeurceramsoc.2020.10.001>
24. E. P. Simonenko, N. P. Simonenko, A. S. Lysenkov, et al., *Russ. J. Inorg. Chem.* **65**, 446 (2020).  
<https://doi.org/10.1134/S0036023620030146>
25. E. P. Simonenko, N. P. Simonenko, V. G. Sevastyanov, et al., *Russ. J. Inorg. Chem.* **64**, 1697 (2019).  
<https://doi.org/10.1134/S0036023619140079>
26. M. Shahriari, M. Zakeri, M. Razavi, et al., *Int. J. Refract. Met. Hard Mater.* **93**, 105350 (2020).  
<https://doi.org/10.1016/j.ijrmhm.2020.105350>
27. V.-H. Nguyen, M. Shahedi Asl, S. A. Delbari, et al., *Ceram. Int.* **47**, 9873 (2020).  
<https://doi.org/10.1016/j.ceramint.2020.12.129>
28. N. Pourmohammadie Vafa, M. Ghassemi Kakroudi, and M. Shahedi Asl, *Ceram. Int.* **46**, 21533 (2020).  
<https://doi.org/10.1016/j.ceramint.2020.05.255>
29. E. P. Simonenko, N. P. Simonenko, A. N. Gordeev, et al., *Russ. J. Inorg. Chem.* **65**, 1596 (2020).  
<https://doi.org/10.1134/S0036023620100198>
30. A. Vinci, L. Zoli, P. Galizia, et al., *J. Eur. Ceram. Soc.* **40**, 5067 (2020).  
<https://doi.org/10.1016/j.jeurceramsoc.2020.06.043>
31. S. Guo, *Adv. Appl. Ceram.* **119**, 218 (2020).  
<https://doi.org/10.1080/17436753.2020.1755510>
32. D. Bannykh, A. Utkin, and N. Baklanova, *Ceram. Int.* **44**, 12451 (2018).  
<https://doi.org/10.1016/j.ceramint.2018.04.035>
33. E. Ghasali and AslM. Shahedi, *Ceram. Int.* **44**, 18078 (2018).  
<https://doi.org/10.1016/j.ceramint.2018.07.011>
34. A. Purwar, V. Thiruvengatam, and B. Basu, *J. Am. Ceram. Soc.* **100**, 4860 (2017).  
<https://doi.org/10.1111/jace.15001>
35. E. P. Simonenko, N. P. Simonenko, V. G. Sevastyanov, et al., *Russ. J. Inorg. Chem.* **63**, 1772 (2018).  
<https://doi.org/10.1134/S003602361814005X>
36. C. Fang, P. Hu, S. Dong, et al., *J. Eur. Ceram. Soc.* **39**, 2805 (2019).  
<https://doi.org/10.1016/j.jeurceramsoc.2019.03.038>
37. D. Sciti, L. Zoli, A. Vinci, et al., *J. Eur. Ceram. Soc.* **41**, 3045 (2021).  
<https://doi.org/10.1016/j.jeurceramsoc.2020.05.032>
38. D. Zhang, P. Hu, S. Dong, et al., *Corros. Sci.* **161**, 108181 (2019).  
<https://doi.org/10.1016/j.corsci.2019.108181>
39. D. Zhang, P. Hu, J. Feng, et al., *Ceram. Int.* **45**, 5467 (2019).  
<https://doi.org/10.1016/j.ceramint.2018.12.001>
40. M. Shahedi Asl, *Ceram. Int.* **43**, 15047 (2017).  
<https://doi.org/10.1016/j.ceramint.2017.08.030>
41. A. Vinci, L. Zoli, E. Landi, et al., *Corros. Sci.* **123**, 129 (2017).  
<https://doi.org/10.1016/j.corsci.2017.04.012>
42. O. Popov, J. Vleugels, E. Zeynalov, et al., *J. Eur. Ceram. Soc.* **40**, 5012 (2020).  
<https://doi.org/10.1016/j.jeurceramsoc.2020.07.039>
43. S. Dubey, S. Awasthi, A. Nisar, et al., *JOM* **72**, 2207 (2020).  
<https://doi.org/10.1007/s11837-020-04164-x>
44. A. Nisar, S. Ariharan, T. Venkateswaran, et al., *Carbon* **111**, 269 (2017).  
<https://doi.org/10.1016/j.carbon.2016.10.002>
45. M. Shahedi Asl, I. Farahbakhsh, and B. Nayebi, *Ceram. Int.* **42**, 1950 (2016).  
<https://doi.org/10.1016/j.ceramint.2015.09.165>
46. J. Lin, Y. Huang, H. Zhang, et al., *Ceram. Int.* **41**, 15261 (2015).  
<https://doi.org/10.1016/j.ceramint.2015.07.207>
47. X. Yue, X. Peng, Z. Wei, et al., *Materials (Basel)* **13**, 370 (2020).  
<https://doi.org/10.3390/ma13020370>
48. A. Wang, H. Liao, T. Zhang, et al., *Int. J. Ceram. Eng. Sci.* **2**, 101 (2020).  
<https://doi.org/10.1002/ces2.10041>
49. N. Pourmohammadie Vafa, M. Ghassemi Kakroudi, and M. Shahedi Asl, *Ceram. Int.* **46**, 8561 (2020).  
<https://doi.org/10.1016/j.ceramint.2019.12.086>
50. M. Shahedi Asl, B. Nayebi, A. Motallebzadeh, et al., *Composites, Part B* **175**, 107153 (2019).  
<https://doi.org/10.1016/j.compositesb.2019.107153>
51. H. Li, Y. Wang, Z. Wang, et al., *J. Micromech. Microeng.* **28**, 105022 (2018).  
<https://doi.org/10.1088/1361-6439/aad79b>
52. Y. Cheng and Y. Liu, Y. An, et al., *J. Eur. Ceram. Soc.* **40**, 2760 (2020).  
<https://doi.org/10.1016/j.jeurceramsoc.2020.03.029>
53. Y. Cheng, Y. Lyu, S. Zhou, et al., *Ceram. Int.* **45**, 4113 (2019).  
<https://doi.org/10.1016/j.ceramint.2018.10.250>
54. Y. Cheng, Y. Lyu, W. Han, et al., *J. Am. Ceram. Soc.* (2018).  
<https://doi.org/10.1111/jace.16068>
55. C. Wei, C. Yu, X. Liu, et al., *Ceram. Int.* **43**, 14493 (2017).  
<https://doi.org/10.1016/j.ceramint.2017.07.063>
56. B. Zhang, X. Zhang, C. Hong, et al., *ACS Appl. Mater. Interfaces* **8**, 11675 (2016).  
<https://doi.org/10.1021/acsami.6b00822>
57. X. Zhang, Y. An, J. Han, et al., *RSC Adv.* **5**, 47060 (2015).  
<https://doi.org/10.1039/C5RA05922D>
58. M. Shahedi Asl, M. Ghassemi Kakroudi, *Mater. Sci. Eng., A* **625**, 385 (2015).  
<https://doi.org/10.1016/j.msea.2014.12.028>
59. M. S. Asl, B. Nayebi, Z. Ahmadi, et al., *Ceram. Int.* **44**, 7334 (2018).  
<https://doi.org/10.1016/j.ceramint.2018.01.214>
60. Y. An, X. Xu, and K. Gui, *Ceram. Int.* **42**, 14066 (2016).  
<https://doi.org/10.1016/j.ceramint.2016.06.014>
61. E. P. Simonenko, N. P. Simonenko, A. F. Kolesnikov, et al. *J. Eur. Ceram. Soc.* (2022).
62. J. Marschall, D. Pejakovic, W. G. Fahrenholtz, et al., *J. Thermophys. Heat Transf.* **26**, 559 (2012).  
<https://doi.org/10.2514/1.T3798>
63. E. P. Simonenko, A. N. Gordeev, N. P. Simonenko, et al., *Russ. J. Inorg. Chem.* **61**, 1203 (2016).  
<https://doi.org/10.1134/S003602361610017X>
64. K. R. Whittle, G. R. Lumpkin, and S. E. Ashbrook, *J. Solid State Chem.* **179**, 512 (2006).  
<https://doi.org/10.1016/j.jssc.2005.11.011>
65. W. H. Zachariasen, *Z. Kristallogr. - Cryst. Mater.* **88**, 150 (1934).  
<https://doi.org/10.1524/zkri.1934.88.1.150>

*Translated by O. Fedorova*